JASA ARTICLE

Bayesian reconstruction of surface shape from phaseless scattered acoustic data

Michael-David Johnson,[1] Jacques Cuenca,[2] Timo Lähivaara,[3] Giulio Dolcetti,[4] Mansour Alkmim,[2,5] Laurent De Ryck,[2] and Anton Krynkin[1,a)]

[1]*Department of Mechanical Engineering, The University of Sheffield, Sheffield, United Kingdom*

[2]*Siemens Digital Industries Software, Interleuvenlaan 68, B-3001 Leuven, Belgium*

[3]*Department of Technical Physics, University of Eastern Finland, Kuopio, Finland*

[4]*Department of Civil, Environmental and Mechanical Engineering, University of Trento, Trento, Italy*

[5]*KU Leuven, Department of Mechanical Engineering, Celestijnenlaan 300 B, B-3001, Leuven, Belgium*

ABSTRACT:

The recovery of the properties or geometry of a rough surface from scattered sound is of interest in many applications, including medicine, water engineering, or structural health monitoring. Existing approaches to reconstruct the roughness profile of a scattering surface based on wave scattering have no intrinsic way of predicting the uncertainty of the reconstruction. In an attempt to recover this uncertainty, a Bayesian framework, and more explicitly, an adaptive Metropolis scheme, is used to infer the properties of a rough surface, parameterised as a superposition of sinusoidal components. The Kirchhoff approximation is used in the present work as the underlying model of wave scattering, and is constrained by the assumption of surface smoothness. This implies a validity region in the parameter space, which is incorporated in the Bayesian formulation, making the resulting method physics informed compared to data-based approaches. For a three-parameter sinusoidal surface and a rough surface with a random roughness profile, physical experiments were conducted to collect scattered field data. The models were then tested on the experimental data. The recovery offers insight of the Bayesian approach results expressed in terms of confidence intervals, and could be used as a method to identify uncertainty.

 https://doi.org/10.1121/10.0034549

(Received 3 June 2024; revised 3 October 2024; accepted 10 November 2024; published online 16 December 2024)

[Editor: Likun Zhang] Pages: 4024–4036

I. INTRODUCTION

Non-intrusive acoustic inversion to recover the elevation or other properties of rough surfaces is an active research field,[1–4] especially in the setting of river monitoring, where intrusive sensors could change the properties of the flow significantly. A numerical method based on the boundary integral equations and Kirchhoff approximation to reconstruct the shape of a scattering surface was outlined in Krynkin *et al.*[5] and Krynkin *et al.*[6] The Kirchhoff approximation is widely used in acoustic reconstruction (see, for example, Joslyn and Dowling[7]) Other methods have risen in inverse scattering, especially in the near-field, such as recovering the scattering coefficients.[8,9] The Kirchhoff approximation approach was found to be highly sensitive to uncertainties, partly because of the strong dependence on the phase of the scattered signal.[10] The review by Ogilvy[11] of methods resolving wave scattering by rough surface highlighted the issue due to shadowing effects at low grazing angles. The work in this paper and the geometry of the experiment ensures that angles are not grazing and the errors in the inversion results were associated with the underdetermined and ill-posed nature of the problem.[10] The range of applicability in reconstructing a surface is also limited by the validity of a partial linearisation of the scattering problem, which is required in order to make the numerical inversion feasible. The method proposed in Krynkin *et al.*[5] was expanded to a multiple frequency approach in Dolcetti *et al.*,[10] and a machine learning approach utilising random forests in Johnson *et al.*[12] Although the performance of these methods has been promising, the statistical measure of the uncertainty is an open question.

Bianco *et al.*[13] presented machine learning in the context of acoustics, with key examples, such as source localisation. Similarly, Andrieu *et al.*[14] introduced Markov–Chain Monte–Carlo (MCMC) methods, providing key theoretical understanding and algorithms for many methods, including Metropolis–Hastings (MH) and Sequential Monte–Carlo.

Bayesian methods have recently gained popularity in the field of acoustics, with applications such as recovering parameters from the seafloor using acoustic backscattering,[15] estimation of rough surface elevation using a Bayesian compressive sensing,[16] and for acoustic holography.[17,18] Li *et al.*[19] applied a MH MCMC scheme to reconstruct the locations and intensities of acoustic sources from near-field and far-field data.

Application of a Bayesian approach for acoustic scattering with phaseless data was proposed by Yang *et al.*[20,21] In

a)Email: a.krynkin@sheffield.ac.uk

https://doi.org/10.1121/10.0034549

Yang *et al.*,[20] the location and shape of a sound-soft scatterer were reconstructed. The approach was tested on shapes, such as kites, disks, and line cracks, with favourable results, noting that the number of parameters being recovered from the MCMC algorithm was no larger than 6. In Yang *et al.*,[21] the method was extended to use a Gibbs sampling method in order to recover more parameters, with phaseless data and a point source excitation. Palafox *et al.*[22] also used a Bayesian formulation in order to reconstruct the shape of a kite, through a reduction of the problem by a Fourier-based representation using a *t*-walk.[23] The effective dimension method was presented where, given a parametric representation of the solution of the inverse problem, the normalising constant can be approximated. Bayesian methods have also been applied in inverse problems in other fields, such as for seismic waveform inversion,[24] and automatic motion analysis in tagged magnetic resonance imaging scans.[25,26]

Application of the adaptive MH scheme in relation to acoustical inverse problems has been presented by Niskanen *et al.*,[27] where the Johnson–Champoux–Allard–Lafarge model was used in conjunction with a MH algorithm in order to recover the model parameters of a homogeneous rigid frame porous media. The joint probability densities verified that the least squares solution was close to the maximum *a posteriori* estimation from the MCMC method. Konarski *et al.*[28] used a similar method, to recover properties from aluminium foams.

The goal of the work is to recover the shape of a rough surface from scattered field. This work shows an application of surface roughness reconstruction based on scattered monochromatic sound recorded with an array of microphones in the far field. The approach incorporates the Kirchhoff approximation into a Bayesian viewpoint, allowing for well-developed sampling schemes, such as the Adaptive Metropolis[29] algorithm to be used to infer the uncertainties of the recovery. The approach is derived and illustrated considering only the magnitude of the scattered field (phaseless data). While the phase distribution is also sensitive to the surface shape, accurate microphone phase calibration can be challenging, especially at high frequencies, and unwrapping issues can lead to multivariate error distributions and lack of robustness of the reconstruction.[10] Phaseless data, in turn, are more easily implemented in a Bayesian framework, and can be easier to measure in some applications. Further, the rough surface is parameterised into a sum of sinusoidal functions, thus potentially reducing the number of parameters to recover, as well as allowing the use of the validity criterion of the Kirchhoff approximation as a constraint. A three-parameter sinusoidal surface presented in Johnson *et al.*[12] is used for verification, as well as a random Gaussian elevation profile used in Dolcetti *et al.*[10] The Gaussian elevation profile is parameterised from a specific Fourier decomposition, where the unknowns of the problem are the amplitude and phase of a number of sinusoidal surface components over a fixed wavelength range.

The paper is organised in the following way: Sec. II presents the parameterisation method of rough surfaces and the theory for the Kirchhoff approximation. Section III proposes a formulation within the Bayesian framework, the MH algorithm, and the approximation for the prior with three-parameter surfaces. Section IV presents an acoustic experiment for the three-parameter and the recovery of a 40-parameter rough surface. Section V presents the results for the recovery of the three-parameter surface, and random 40-parameter rough surface with a flat surface as an initial condition. This is followed by discussions on efficiency of the inversion algorithm. Section VI concludes the report.

II. FORWARD MODEL OF ACOUSTIC SCATTERING

The work in this paper in concerned with estimating roughness parameters given scattered acoustic data. This scattered acoustic data will be used as input to the model described in Sec. III A. The outputs to the model will be roughness parameters relating to the amplitude, wavelength, and phase of various harmonic components. This approximation is done to reduce the number of parameters needed to infer and approximate the shape of the surface of interest. Defining N harmonics of the surface through parameters $\theta = \{\theta_j | j = 1, \ldots, 3N\}$, a surface profile can be expressed as

$$\zeta(x, \theta) = \sum_{i=0}^{(N-1)} \theta_{3i+1} \cos\left[\frac{2\pi x}{\theta_{3i+2}} + \theta_{3i+3}\right], \tag{1}$$

where the triplet $(\theta_{3i+1}, \theta_{3i+2}, \theta_{3i+3})$ represents the amplitude, wavelength, and phase of the i-th harmonic. The approach was tested on two types of rough surfaces, which are fully described by a different number of parameters: a sinusoidal surface (three parameters) and a random surface (40 parameters). The acoustic signal was recorded at a set of M microphones with coordinates of the j-th microphone given by $\mathbf{R}^{(j)} = \{(x_2^{(j)}, y_2^{(j)}) | j = 1, \ldots, M\}$.

The Kirchhoff approximation was chosen due to its ability to represent the scattered field in an explicit form, obtained with the assumption based on reflections from a tangent plane. This closed form enables fast calculations, as opposed to the full boundary integral equation solution, for instance. The suitability of this approximation for the conditions analysed in this paper was presented in Krynkin *et al.*[5] and Krynkin *et al.*[6] The problem is stated in two-dimensional Oxy semi-infinite domain and for time harmonic dependence $\exp(-i\omega t)$.

The domain is bounded by the rough surface $\zeta(x, \theta)$ defined with Eq. (1). The surface $\zeta(x, \theta)$ satisfies the Kirchhoff approximation condition given by Thorsos,[30]

$$\sin(\phi(x)) > \frac{1}{(kh(x))^{1/3}}, \tag{2}$$

where $h(x)$ is the radius of curvature of the surface, k is the acoustic wavenumber, and $\phi(x)$ is the angle of incidence of the acoustic wave relative to the horizontal axis. Assuming

separation of variables, with the condition (2) satisfied and for a source with a given directivity pattern at a given point on the surface $A(x, \zeta(x,\theta))$, the scattered field ψ_s in the frequency domain can be expressed in the following equation:[6]

$$\psi_s(\mathbf{R},\theta) = \frac{1}{2k\pi \mathrm{i}} \int_{-\infty}^{\infty} \frac{A(x,\zeta(x,\theta)}{\sqrt{R_1 R_2}} \times \exp(\mathrm{i}k(R_1+R_2))(q_y - q_x\gamma)\,\mathrm{d}x, \tag{3}$$

where, as shown in Fig. 1, the values R_1 and R_2 are the Euclidean distances from the source at (x_1, y_1) and receiver at (x_2, y_2) to a given point $(x, \zeta(x,\theta))$ on the surface, respectively,

$$R_1 = \sqrt{(x_1 - x)^2 + (y_1 - \zeta(x,\theta))^2}, \tag{4}$$

$$R_2 = \sqrt{(x_2 - x)^2 + (y_2 - \zeta(x,\theta))^2}. \tag{5}$$

In Eq. (3), $\mathbf{R} = (x_2, y_2)$, $\gamma = \mathrm{d}\zeta(x,\theta)/\mathrm{d}x$; q_x and q_y are the x and y components of $\mathbf{q} = -k\nabla_S(R_1 + R_2)$, $\nabla_S = (\partial/\partial x, \partial/\partial y)$. The directivity term $A(x)$ is defined in this work as the far-field radiation from a baffled piston, which is given by[31]

$$A(x) = \frac{2J_1(ka\sin(\phi(x) + \phi_0))}{ka\sin(\phi(x) + \phi_0)}, \tag{6}$$

where a is the aperture (approximated experimentally as 0.018), $J_1(\cdot)$ is the Bessel function of the first kind, ϕ_0 is the angle of inclination of the source main axis to the Ox-axis, and $\phi(x)$ is the angle between the vector defined by the location of the source and a point x on the projected line with a unit vector parallel to the Oy-axis. It is noted that the use of the baffled piston directivity pattern originally derived for three-dimensional problems is used in this study to relate the predictions with data collection method introduced in Sec. IV. This includes parameterisation of the source (i.e., true radius of the source aperture) and resulting width of the acoustic incident wave.

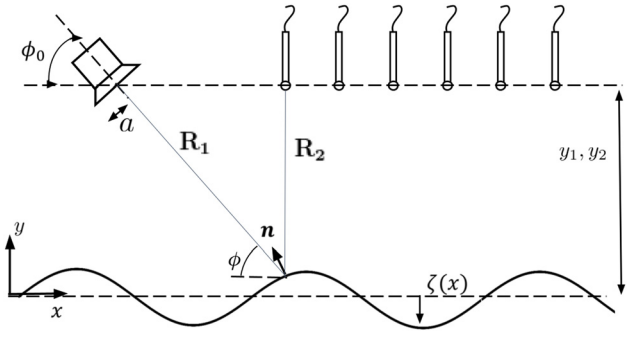

FIG. 1. (Color online) The geometry of the problem where the rough surface is defined by a function $\zeta(x)$ from Eq. (1). Surface is not to scale. On the top right of the image, there is a pictorial representation of the linear array of microphones which could be at a different height y_2 than the height of the source y_1.

Following the application of the Kirchhoff approximation to simulate the scattered field, the phase is removed from Eq. (3) through the application of the modulus

$$p(\mathbf{R},\theta) = |\psi_s(\mathbf{R},\theta)|. \tag{7}$$

Taking into account the receiver locations in an array of M receivers, phase-removed scattered field is given by the following matrix:

$$\mathbf{p}(\theta) = \{p(\mathbf{R}^{(j)},\theta)|\, j = 1,\ldots,M\}, \tag{8}$$

where the matrix is formed from $p(\mathbf{R}^{(j)},\theta)$ (an ensemble containing the array of magnitudes of the scattered field for a given surface profile ζ) with $\mathbf{R}^{(j)}$ forming an array of receiver locations defined with respect to the origin of the Oxy plane.

The Kirchhoff approximation model is deterministic; therefore, one set of surface parameters maps to a given scattered field. However, in practical applications, noise and modelling errors are present. It is proposed to modify the solution of the Kirchhoff approximation via additive noise, calculated as

$$\tilde{\mathbf{p}}(\theta) = \mathbf{p}(\theta) + \boldsymbol{\epsilon}, \tag{9}$$

where $\boldsymbol{\epsilon} = \epsilon_j | j = 1,\ldots,M$, with $\epsilon_j \sim \mathcal{N}(0,\sigma)$ represents deviation from the Kirchhoff model via environmental noise and modelling errors. It is drawn from a normal distribution independently for each receiver with mean 0 and standard deviation σ.

III. INVERSE PROBLEM

A. Bayesian framework

One approach to Eq. (9) is to treat the overall equation in the perspective of probability. As $\boldsymbol{\epsilon}$ is drawn from a probability distribution, Eq. (9) motivates the application of Bayes's theorem:[32]

$$\mathcal{P}(\theta|\tilde{\mathbf{p}}) \propto \mathcal{P}(\tilde{\mathbf{p}}|\theta)\mathcal{P}(\theta). \tag{10}$$

The left-hand side is referred to as the posterior distribution and allows for distributions to be taken over parameters θ given a measurement $\tilde{\mathbf{p}}$, $\mathcal{P}(\tilde{\mathbf{p}}|\theta)$ is called the likelihood function, which is the probability of the observed acoustic scattered field given the model parameters, and $\mathcal{P}(\theta)$ is called the prior distribution and encompasses prior belief on the distribution of parameters. In the present paper, the prior distribution is defined from the Kirchhoff approximation condition, as detailed further below.

With the Gaussian noise in the observation model [Eq. 9)], the likelihood $\mathcal{P}(\tilde{\mathbf{p}}|\theta)$ can be written as

$$\mathcal{P}(\tilde{\mathbf{p}}|\theta) = f_{MN}(\tilde{\mathbf{p}}, \theta, \boldsymbol{\Sigma}) \tag{11}$$

with

https://doi.org/10.1121/10.0034549

$$f_{MN}(\tilde{\boldsymbol{p}}, \theta, \boldsymbol{\Sigma}) = \frac{\exp\left\{-[\tilde{\boldsymbol{p}} - \mathbf{p}(\theta)]^T \boldsymbol{\Sigma}^{-1} [\tilde{\boldsymbol{p}} - \mathbf{p}(\theta)]/2\right\}}{\sqrt{(2\pi)^k |\boldsymbol{\Sigma}|}}, \tag{12}$$

where f_{MN} is a multivariate Gaussian probability density function and $\boldsymbol{\Sigma}$ is the covariance matrix representing the error $\boldsymbol{\epsilon}$ added to each receiver. In the present work, the error in the scattered field is assumed uncorrelated across receivers and therefore the covariance matrix is assumed to be diagonal.

B. Posterior sampling algorithm

In this work, the MH algorithm is used for sampling the posterior distribution and drawing new potential states from the state space, where the posterior distribution is obtained adaptively by updating the proposal distribution to target a specific acceptance rate.[29,33] The proposal distribution determines the probability of moving the samples in the trace, and the construction is given by Haario *et al.*[29] A key piece of literature in understanding various MCMC methods, including the method used in this work, is given in Andrieu and Thoms[34] and Kaipio and Somersalo[35] As an initial state, the surface is considered flat, both in the three-parameter and 40-parameter problems. For every iteration, a uniform random number between zero and one is generated in order to randomly accept or reject a proposed sample. The proposed sample is drawn from the proposal distribution and the posterior distribution calculated. A ratio (known as the acceptance ratio) is calculated from the posterior of the proposed sample, divided by the posterior of the current sample. If the posterior of the proposed sample is greater than the posterior of the previous sample, then the acceptance ratio is greater than 1, guaranteeing that the proposed sample is accepted. If the ratio is greater than zero and less than 1, then the uniformly generated random number is used to reject or accept the proposed sample. Typically, the collection of accepted and rejected samples is referred to as the trace, and the trace tends to settle to the stationary distribution. Removing that transitional period at the start of the trace is referred to as removing the "burn-in" period. The reader can find a more detailed description of the MH algorithm in Kaipio and Somersalo.[35]

C. An approximation for three-parameter recovery

For three-parameter recovery, the scattering surface is fully defined by the surface amplitude, $\theta_{1;}$ surface wavelength, $\theta_{2;}$ and surface phase, θ_3. The Kirchhoff condition (2) depends on the acoustic wavelength λ. The Kirchhoff condition for a given source excitation frequency at a given acoustic wavenumber, surface amplitude, and angle of incidence can be approximated with the following expression:

$$\theta_2 > \sqrt{\frac{(2\pi)^2}{k \sin^3(\phi)} |\theta_1|} = \beta. \tag{13}$$

The surface amplitudes θ_1 is further restricted by constraining the maximum surface amplitude to be $y_s - 3\lambda$ as a bound to guarantee that scattered field will be given at the far-field. Assuming a maximum allowed wavelength value $\theta_{2,\max}$, this gives a closed interval of surface parameters that satisfy the Kirchhoff criteria in amplitude-wavelength space, allowing for a prior (assuming uniform prior)

$$\mathcal{P}(\theta) = f(\theta_1, \theta_2)\mathcal{U}(0, 2\pi), \tag{14}$$

where $\mathcal{U}$ is the uniform distribution for the phase θ_3 between 0 and 2π, and $f(\theta_1, \theta_2)$ is the conditional uniform distribution of θ_1 and θ_2 over the domain of Kirchhoff criteria satisfaction given by

$$f(\theta_1, \theta_2) = \begin{cases} \left[\int_{-(y_s - 3\lambda)}^{y_s - 3\lambda} \int_{\beta}^{\theta_{2,\max}} 1 \, \mathrm{d}\theta_2 \, \mathrm{d}\theta_1\right]^{-1} & \text{if} \quad |\theta_1| \le y_s - 3\lambda, \ \beta \le \theta_2 \le \theta_{2,\max}, \\ 0 & \text{otherwise.} \end{cases} \tag{15}$$

Therefore, for the three-parameter case, the prior can be evaluated analytically. For higher dimensional cases, the Kirchhoff condition needs to be evaluated numerically for every step in the MCMC scheme. In the case of the 40-parameter recovery for this research, the surface is determined as the sum of 20 sinusoids, each one represented by three parameters (amplitude, wavelength, and phase). In this case, the prior on the amplitude and phase parameters we draw from a uniform distribution. To ensure that the surface realisations satisfied the Kirchhoff criterion, the prior was set to zero if the condition failed.

To measure the accuracy of the recovered surface parameters, two-surface types were generated from the prediction step. The first type of surface [referred to as $\zeta(x, \bar{\theta})$] was found by substituting the mean of the resultant surface parameters $\bar{\theta}$ obtained from the trace of the MH scheme, namely the conditional mean. The second kind of surface [referred to as $\overline{\zeta(x, \theta)}$] was found by averaging surfaces generated by the parameters along the spatial direction.

IV. DATA COLLECTION

In order to validate the surface reconstruction methodology, scattered field was recorded by a set of 34 1/4″

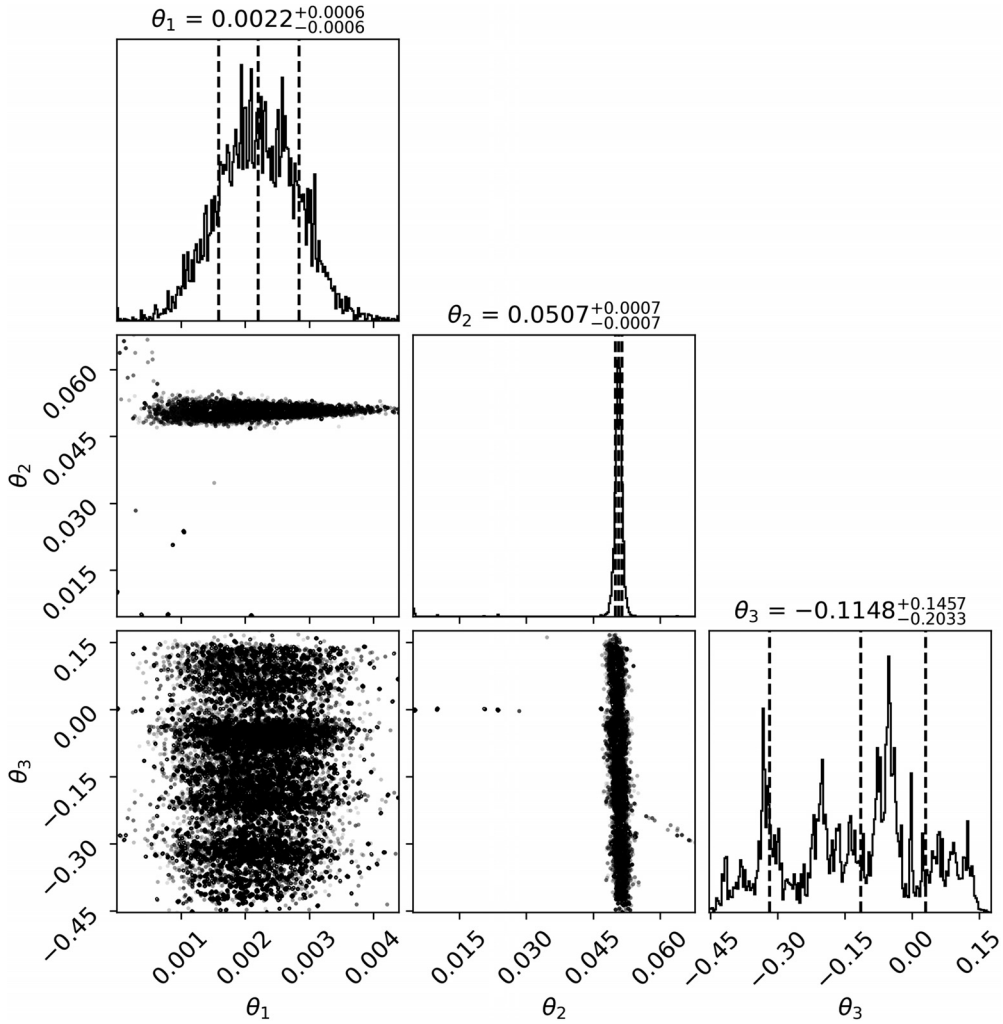

FIG. 2. Corner plot of the distribution of the traces for the amplitude [θ_1 (m)], wavelength [θ_2 (m)], and phase [θ_3 (rads)] for the three-parameter surface. The subtitles contain the mean and the 68% credible interval bounds.

microphones (G.R.A.S. 40PH) above two acoustically rigid surfaces with known profiles described in Dolcetti *et al.*[10] A white noise signal was produced with a loudspeaker (Visaton G 25 FFL) and recorded simultaneously at all microphones, with a sampling frequency of 102.4 kHz. Arrangement of both speaker and array of microphones is identical to that described in Johnson *et al.*[12] The signal amplitude at each microphone was calculated by a Fourier transform applied to 0.02 s–long segments of the signal using a Hann window, and then averaged over 2000 segments. The data were calibrated *in situ* by comparing measurements of the sound field reflected by a flat surface with the corresponding prediction calculated numerically, following the procedure outlined in Dolcetti *et al.*[10] The calibrated experimental data and the simulated received scattered field were then divided by the maximum value of the simulated absolute scattered field from a flat surface. This procedure increased the measured response from all receivers by a scaling factor, which improved convergence speed in the inversion process. The signals used for the three-parameter surface had a frequency of 14 kHz (which corresponds to a minimum kR_1 value of 56.12 and minimum kR_2 value of 72.58) to compare with the results presented in Johnson *et al.*[12] The signal used for the 40-parameter analysis had a frequency of 18.6 kHz (which corresponds to a minimum kR_1 value of 70.03 and minimum kR_2 value of 91.92).

One surface profile was milled on the upper face of an aluminium block with horizontal dimensions 0.55 $\times$ 0.35 m^2. The profile was sinusoidal along the longer dimension, with a wavelength of 50 mm and a peak-to-peak amplitude of 3 mm, and was constant along the shorter dimension. The second profile was milled onto a block of medium-density fiberboard (MDF) with dimensions of 0.6 $\times$ 0.4 m^2. This profile was generated via Fourier synthesis,[30] i.e., as a random realisation of a surface with discrete spatial power spectrum $\Psi(K_i)$ expressed as a function of the wavenumber $K_i = i2\pi/L$, where L is the surface length

$$\zeta_{\exp}(x) = \sum_{i=0}^{N/2} \sqrt{2\Psi(K_i)}\mathcal{N}(0,1)\cos(K_i x - \mathcal{U}(0,2\pi)), \qquad (16)$$

https://doi.org/10.1121/10.0034549

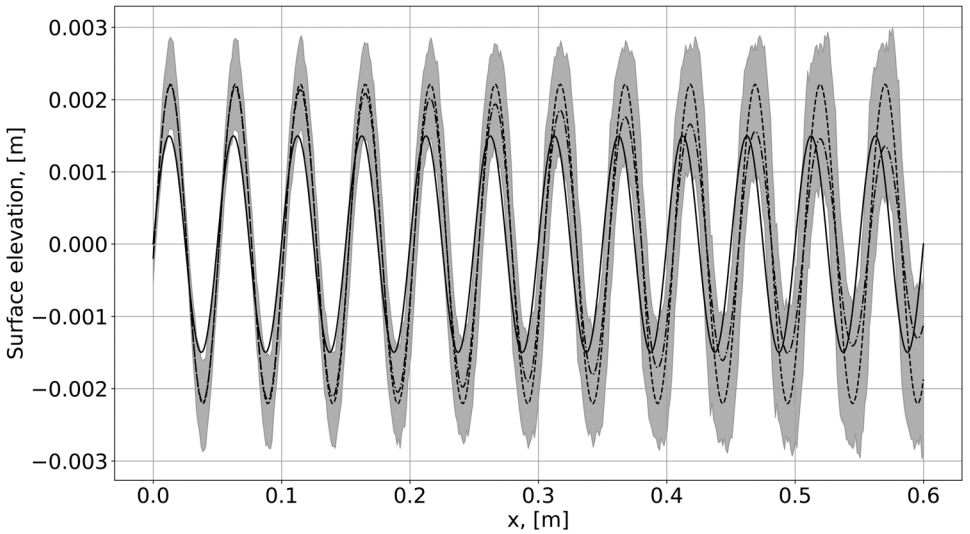

FIG. 3. Surface elevation of the three-parameter surface. True geometry (solid line); surface $\zeta(x,\bar{\theta})$ generated from the conditional mean of MCMC parameter samples (dashed line); mean of all surfaces $\overline{\zeta(x,\theta)}$ obtained from MCMC parameter samples (dashed-dotted line); 68% credible interval (shaded region).

where $\mathcal{N}(0,1)$ indicates a sample from a normal distribution, and $\mathcal{U}(0,2\pi)$ indicates a sample from a uniform distribution in the interval $(0,2\pi)$. This representation is directly linked with the surface parameterisation described by Eq. (1). The power spectrum is proportional to the squared amplitude of the i-th surface harmonic with wavelength $2\pi/K_i$. Here, $\Psi(K_i)$ was assumed to vary like a power function of the wavenumber, $\Psi(K_i) \propto K_i^{-\alpha}$, which is representative of natural surfaces, such as the water surface or the bed surface of rivers or of the oceans.[36–39] Here, the surface had $\alpha = 5$, in agreement with experimental observations of the water surface of open-channel flows.[40] To ensure the integrability of the spectrum, a saturation range at low wavenumbers $K_i < 2\pi/0.05$ rad m^{-1} was introduced following Stewart *et al.*,[39] i.e., $\Psi(K_i < 2\pi/0.05) = \Psi(2\pi/0.05)$. The spectrum had a small-scale cutoff at $K_i > 2\pi/0.01$ rad m^{-1}. The standard deviation of the random surface height was equal to 1 mm and the surface satisfied the Kirchhoff condition.

V. RESULTS

A. Three-parameter recovery

For the three-parameter surface, the algorithm ran for 1 00 000 samples. The burn-in period was set at 10 000 samples, and the covariance matrix was updated every 20 samples. The values of the standard deviation were set as $\sigma = 0.15\bar{p}(\mathbf{R})$ where $\bar{p}(\mathbf{R})$ is the mean scattered field received along the linear array according to the simulations described by Johnson *et al.*[12] for the same geometry and frequency was set to be 15% error of the mean scattered field from the Kirchhoff approximation of the true surface to match Table II in Johnson *et al.*[12] The targeted acceptance ratio was 20%.

Figure 2 presents a corner plot generated with the method outlined in Foreman–Mackey *et al.*[41] The leading diagonal contains histograms with a distribution of occurrences of each parameter, with the vertical dashed lines

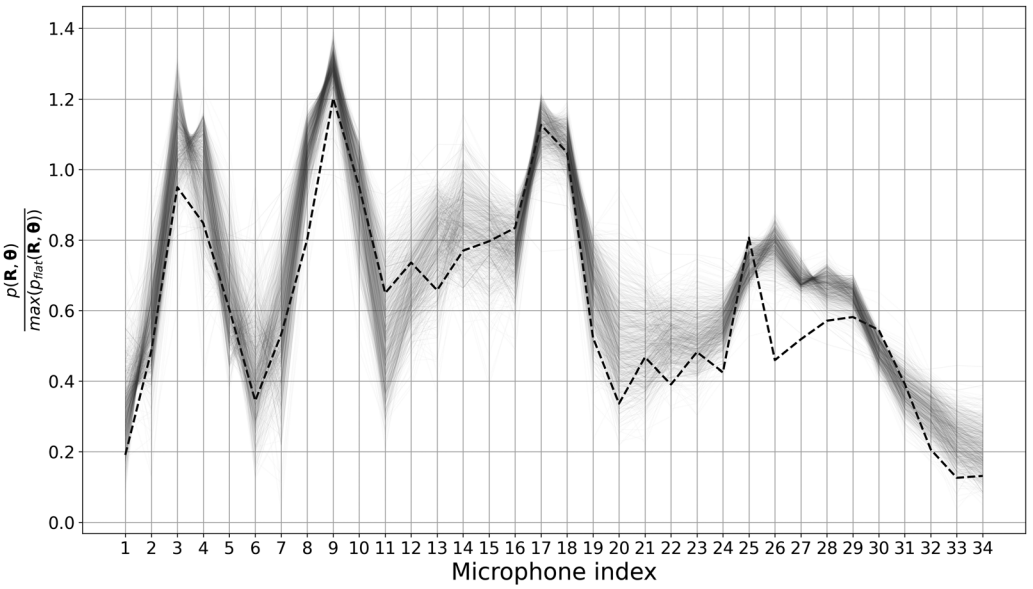

FIG. 4. 1000 random samples of the trace (shaded region), plotted against the real data (dashed line) for the three-parameter surface recovery.

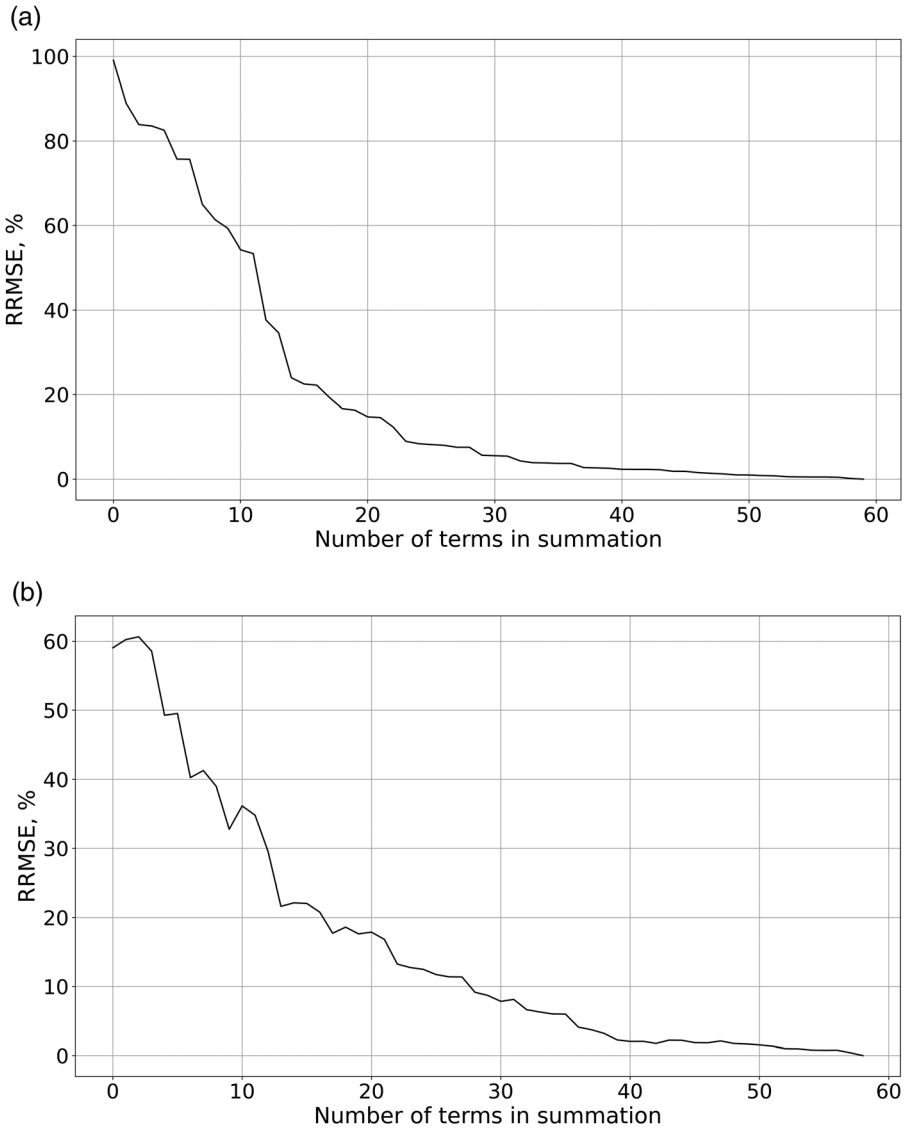

FIG. 5. (a) Relative root-mean-square error (RRMSE) of the true surface against a truncated version of the surface, (b) RRMSE of the acoustic field amplitude calculated for the true surface and for a truncated version of the surface defined by the summation of a smaller number of terms.

representing the 68% credible interval (i.e., an interval that contains 68% of the probability mass: the first vertical line is the lower bound, the second is the mean, and the third is the upper bound). The wavelength parameter θ_2 is highly accurate, with approximately 1% error from the true wavelength at the mean of the distribution. The amplitude parameter θ_1 is overestimated by 0.7 mm, and the spread is large. The scatter plots represent the two-dimensional marginal probability distributions, which highlights that the variability in surface phase has a larger impact on the uncertainty of the surface amplitude compared to the surface wavelength.

Figure 3 presents the comparison between the surface obtained from the conditional mean of each parameter in the trace $\zeta(x, \bar{\theta})$, the mean of all the surfaces generated from the distribution of parameters $\overline{\zeta(\mathbf{x}, \theta)}$, and the 68% credible interval. $\zeta(x, \bar{\theta})$ and $\overline{\zeta(\mathbf{x}, \theta)}$ were very close to each other in the region of the most insonified area when x is between 0.1 and 0.3 m. In this region, the recovered surfaces have highest accuracy in relation to the original three-parameter surface. Outside this region, the accuracy of the spatial reconstruction degrades due to the errors in the wavelength. This behaviour is replicated in the credible interval, where the shaded region widens further away from the region of specular reflection of the directivity pattern [Eq. (6)] mainlobe.

For the case of the mean surface $\overline{\zeta(\mathbf{x}, \theta)}$, the amplitude decreases as the x coordinate increases. This is due to the variation in both amplitude and wavelength.

Figure 4 presents the scattered field from 1000 random samples from the trace. The peaks in the absolute scattered field are well mapped (especially around indexes 9, 17, and 18), as the random samples from the trace converge to the peaks. There is a tendency for the traces to overestimate the true scattered field, most notable with receivers 2–5 and 25–30. The regions where the absolute scattered field does not change much, such as in regions between receivers 10 and 15, contain more uncertainty, which can be seen from the increased variability of the traces. The traces appear to be less scattered at the tail end of the receivers, but do not match the experimental scattered field at receivers 25–28.

https://doi.org/10.1121/10.0034549

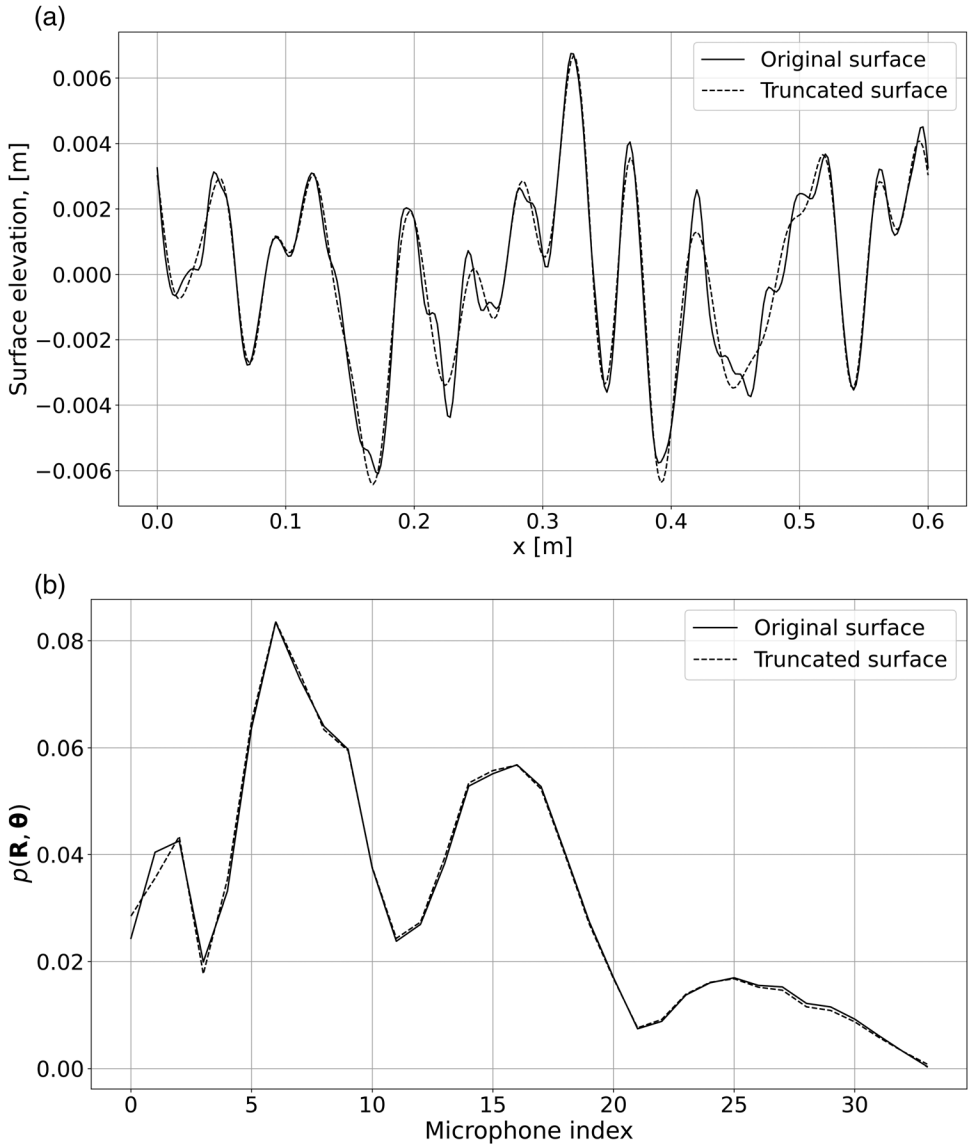

FIG. 6. Comparison of the second rough surface profile against the truncated sum of 20 sinusoidal waves for (a) the surface elevation, (b) the corresponding Kirchhoff approximation.

The uncertainty increases around receivers 11–15 and 19–13. This uncertainty provides information that the receivers in this location contributed less to the scattered field, and could be used as a method to dynamically reshape the linear array.

In order to benchmark the performance of this method for the three-parameter recovery, the results from Johnson *et al.*[12] are used for comparison. With a random forest recovery trained on the three parameters with 15% additive Gaussian white noise, the results for the amplitude, wavelength, and offset (defined as the phase divided by the wavelength) in Johnson *et al.*[12]) are 0.001 42, 0.0516, and –0.001 94 m.[12] The wavelength (≈0.0507 m) and offset (≈−0.000 93 m) for the proposed method at the mean have improved compared to those from Johnson *et al.*[12] The error of the mean amplitude was larger than in Johnson *et al.*[12] Yet, the results from the random forest were within the uncertainty bounds calculated with the method presented here. The further knowledge to be gained from the uncertainty bounds over the parameters is useful in showing which parameter causes the most uncertainty, the amplitude θ_1.

B. 40-parameter recovery

To further test the adaptive Metropolis scheme, the scattering of the acoustic signal was studied over the surface referred to as second surface profile in Sec. IV. For the computation and the prediction of the parameters, this surface was described in terms of a truncated Fourier spectrum following Eq. (1), where the amplitude and phase of each Fourier mode represented the unknown parameters and the wavelengths were fixed and known. To reduce the number of parameters to recover, the spectrum of the surface was truncated and rank ordered by the largest wavelength to the smallest wavelength (see Appendix A). In order to select a viable reduction of the terms in the summation, the relative

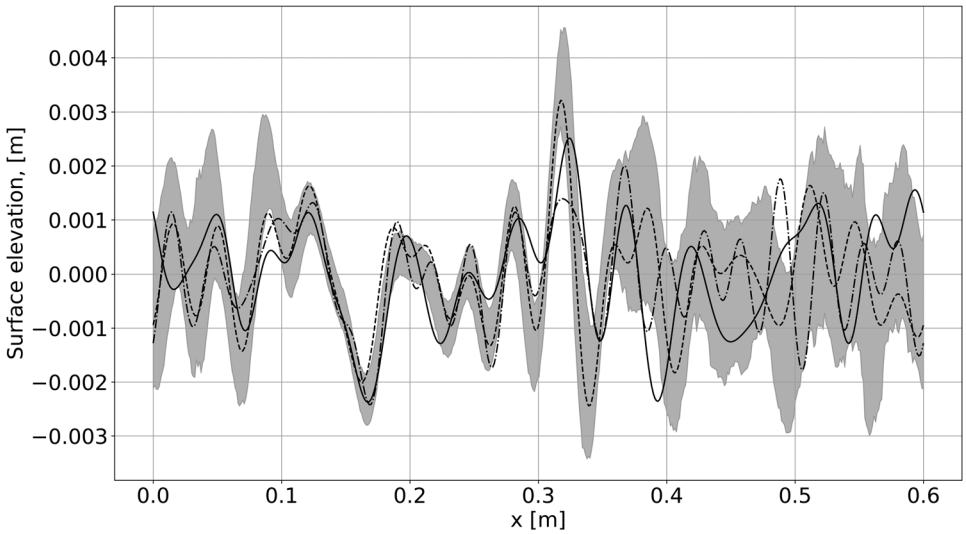

FIG. 7. Surface elevation of the 40 parameter surface. True geometry (solid line); surface $\zeta(x, \bar{\theta})$ generated from the conditional mean of MCMC parameter samples (dashed line); mean of all surfaces $\overline{\zeta(x, \theta)}$ obtained from MCMC parameter samples (dashed-dotted line); 68% credible interval (shaded region).

root mean square error (RRMSE) of the reduced surface was compared to the true surface. Additionally, the RRMSE of the resultant Kirchhoff approximation scattered field solution from the reduced surface in comparison to the Kirchhoff approximation solution using the true surface was also compared. For both the metrics, a normalisation based on the standard deviation was applied.

In Fig. 5(a), the results were normalised by the standard deviation of the full surface, and in Fig. 5(a), the results were normalised by the standard deviation of the Kirchhoff approximation solution found from scattering from the full surface. Both RRMSE exceeds 10% and increases rapidly at truncations below 20 terms. Therefore, a truncation of 20 terms was selected, which corresponded to recovering 40 parameters. The resulting approximations of the surface and the Kirchhoff approximation are shown in Fig. 6. The corresponding parameters are contained in Table I and can be found in Appendix A.

For the 40-parameter case, the Adaptive Metropolis scheme was used, running for 5 00 000 samples. The error for the likelihood function was set at 0.1, which relates approximately to the root-mean-squared error between the Kirchhoff approximation of the true surface, and the experimental noise (≈0.909). This value corresponds to an error of approximately 17% of the mean scattered field obtained from the Kirchhoff approximation. The burn-in period was set at 50 000 samples, and the covariance matrix was updated every 50 samples. The acceptance rate was reduced to 10%. The phase parameter in the MCMC was not allowed to increase more than 2π, and this was achieved by restricting the value to the region $(0, 2\pi)$. This causes wrapping of the phase parameters in the trace. This is accounted for in the angular mean metric as shown in Appendix B, which is used throughout this work. It is noted that the periodicity condition maintains ergodicity of the Markov–Chain and therefore, the MCMC approach is valid for the phase constrained in the region $(0, 2\pi)$.[14]

Due to the substantially increased number of parameters, a corner plot similar to that in Fig. 2 is not shown here. Similar to the three-parameter surface, the MH scheme was

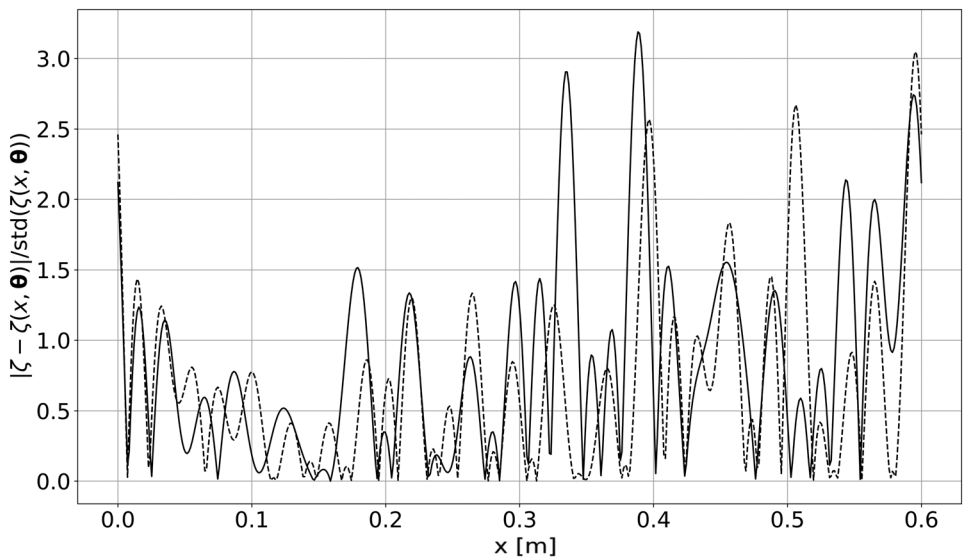

FIG. 8. Spatial variation of the relative error for the surface $\zeta(x, \bar{\theta})$ of the mean of each parameter in the posterior (solid line), and the mean of the resulting surfaces $\overline{\zeta(x, \theta)}$ (dashed line), against the true surface factored by the standard deviation of the true surface.

https://doi.org/10.1121/10.0034549

initialised with a flat surface. Figure 7 presents the results with a 68% credible interval obtained via the highest posterior density interval. The mean predictions closely match the exact solution from the experiments in the central region of the directivity pattern defined by Eq. (6) $x \in [0.1, 0.3]$, then begins to deviate from the true surface outside that region. The uncertainty from the model is shown in the gray filled region and represents the solution traces from the 68% credible interval. The width of the 68% credible interval decreases for $x \in [0.1, 0.3]$. This is consistent with the results obtained for the three-parameter surface (see Fig. 3) and conclusions made for the surface reconstruction interval in Dolcetti *et al.*[10] The credible interval also highlights that in the areas outside the central region, the inversion algorithm becomes more uncertain. This is expected as the information in the scattered signal is dominated from the high insonification region.

Figure 8 highlights the absolute error for both the mean surface predictions (defined as ζ in the label for the vertical axis of the graph) compared against the true surface $\zeta(x, \theta)$. In the region of high insonification (relating to $x \in [0.1, 0.3]$), the mean of the surfaces $\overline{\zeta(x, \theta)}$ is closer to the true surface than the surface generated by the mean of the parameters $\zeta(x, \bar{\theta})$, and the average error for both predicted mean surfaces is below 1.5 standard deviation of the original ground truth surface.

Figures 9 and 10 present histograms of the amplitude parameters of a few surface terms from the traces of MCMC parameter samples, and elevation of the reconstructed surfaces evaluated at a discrete set of points (the two end points, as well as $x = 0.12$ and $x = 0.3$), respectively. Due to the large amount of parameters, a subset was taken for visualisation. It is also noted that the distribution of the amplitude parameters becomes uniform as the wavelength increases, which highlights almost equivalent contribution of the large surface scales within the given range of the parameters to the scattered acoustic wave. The histograms from the surface elevations (Fig. 10) result in a Gaussian shape compared to those for the amplitude parameters.

VI. CONCLUSION

The purpose of the paper was to reconstruct a rough surface from acoustic scattering and to obtain a measure of the uncertainty, highlighted in Figs. 7–10. The methodology can be used on its own, or as a means to extend non-stochastic methods, such as previous work by the authors using random forests.[12] In this paper, the MH algorithm was used in order to treat the set of parameters that form a parameterisation of the surface elevation function as a posterior distribution. This posterior distribution can then be queried to get a credible interval, as a measure of uncertainty. The model was tested on two surfaces, a single sinusoidal surface parameterised with three parameters, and a rough surface composed of multiple harmonics dependent on 40 parameters (amplitudes and phases) and where the wavelengths were fixed. Laboratory measurements were taken to acquire the scattered field. The prior was decided to be uniform, and the Kirchhoff criterion was inserted into the prior to inform the model of the physics. The results for the mean surface acquired from the mean of each parameter were highlighted as a model prediction. The mean

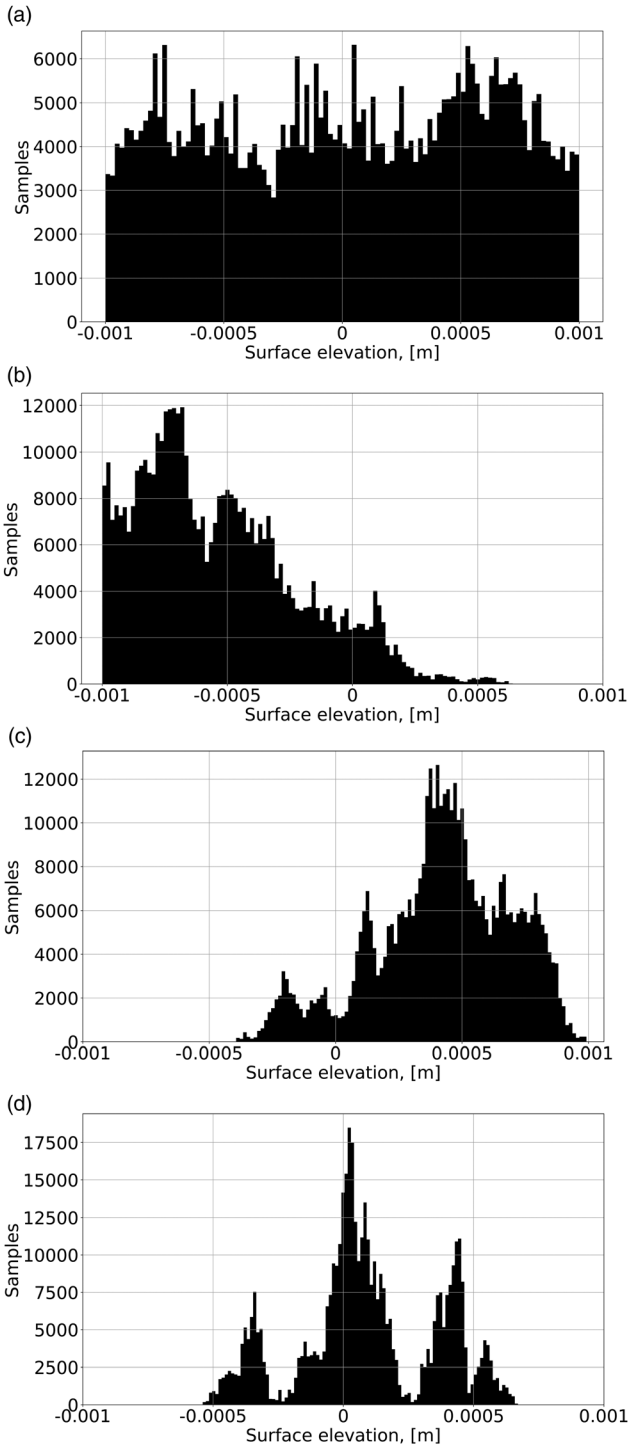

FIG. 9. Histograms of the traces (excluding the burn-in period) of the amplitude parameters defined by Eq. (1) for (a) the first surface term, (b) the seventh surface term, (c) the ninth surface term, (d) the 14th surface term.

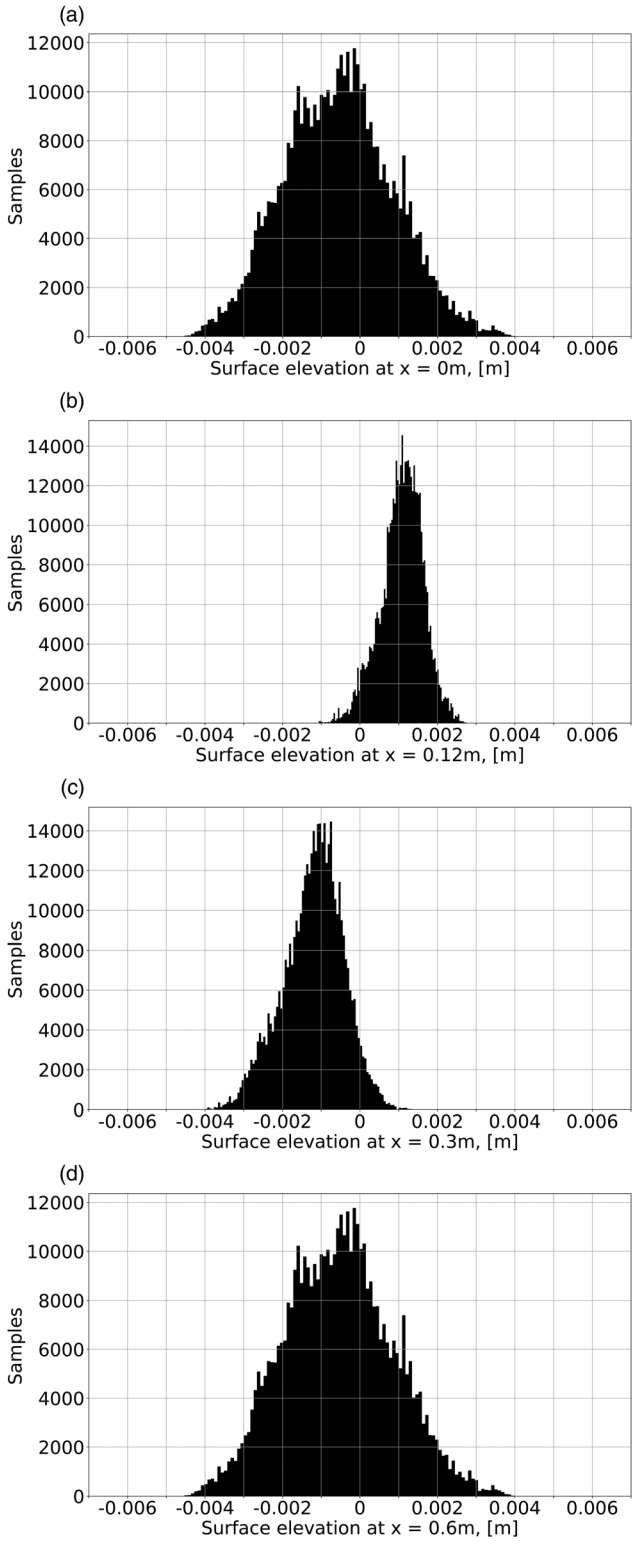

FIG. 10. Histograms of the surface elevation from the collection of surfaces generated from the MCMC traces (excluding the burn-in period) for (a) $x = 0$ m, (b) $x = 0.12$ m, (c) $x = 0.3$ m, (d) $x = 0.6$ m.

surface generated for both the three- and the 40-parameter surfaces had good agreement, especially in the region of high insonification, when compared against the ground truth. The credible intervals highlighted the region where the model uncertainty is lower. This interval is also consistent with the underlying physics, as the scattered field will be most affected by the surface roughness in the region of high insonification The errors in the predictions were quantified through the application of the absolute error factored by the true surface standard deviation, and this was tested with the two types of mean surfaces that can be recovered with the proposed method using a parameterisation of the surface. The method of obtaining a mean surface by taking the mean at each spatial point for $x \in [0.1, 0.6]$ for the complete set of surfaces generated with the distribution of parameters outperformed the method of taking the mean for each parameter, then generating one surface, over the majority of the region. The results showcase the promising aspect of including the credible interval. Further extensions to this work include varying the spatial wavelength of the surface. In this work, the surface wavelengths were fixed due to the assumption that surfaces were following the Fourier decomposition. However, these fixed spatial wavelengths could have been a distribution themselves that removes the need for a prior assumption on the Fourier decomposition of the surface. Also, the application of a more accurate optimiser or a comparison of different optimisers to form an initial guess on the surface[42] could be an extension of an initial surface condition, allowing for a shrinking or extending of the credible region. Finally, as the number of parameters that represent the surface (such as including more terms in the summation, or directly inferring surface elevations along the length of the reflecting rough surface) increase, methods such as Hamiltonian Monte-Carlo[43] may provide more favourable results due to the increase in MCMC search space.

ACKNOWLEDGMENTS

This work was partially supported by the UK EPSRC Grant No. EP/R022275/1 and Knowledge Exchange Support Fund provided by the UK Engineering and Physical Sciences Research Council (EPSRC). The authors would like to acknowledge the support of the Research Council of Finland via the Finnish Centre of Excellence of Inverse Modelling and Imaging, Flagship of Advanced Mathematics for Sensing, Imaging, and Modelling (Grant No. 358944), and project (Grant No. 321761). M.-D.J. would like to acknowledge the support of the University of Sheffield through their Ph.D. studentship award.

AUTHOR DECLARATIONS

Conflict of Interest

The authors have no conflicts to disclose.

DATA AVAILABILITY

The data that support the findings of this study are available from the corresponding author upon reasonable request.

https://doi.org/10.1121/10.0034549

TABLE I. Parameters that define the truncated surface representing the overall surface.

Surface term	Amplitude (m)	Wavelength (m)	Phase	Surface term	Amplitude (m)	Wavelength (m)	Phase
1	-1.86×10^{-4}	0.6	3.42	11	3.37×10^{-4}	0.055	1.70
2	6.11×10^{-4}	0.3	6.21	12	-1.44×10^{-4}	0.05	0.29
3	4.22×10^{-4}	0.2	2.82	13	-5.33×10^{-4}	0.046	2.62
4	9.95×10^{-5}	0.15	5.82	14	-2.11×10^{-4}	0.043	5.19
5	1.83×10^{-4}	0.12	0.90	15	3.52×10^{-4}	0.04	5.54
6	4.62×10^{-4}	0.1	5.64	16	1.17×10^{-4}	0.038	0.87
7	-3.93×10^{-5}	0.089	5.35	17	-4.99×10^{-5}	0.035	5.33
8	5.50×10^{-4}	0.075	2.081	18	1.56×10^{-4}	0.033	1.79
9	-3.03×10^{-4}	0.067	4.86	19	1.36×10^{-4}	0.032	1.66
10	2.22×10^{-4}	0.06	4.98	20	4.88×10^{-5}	0.03	1.059

APPENDIX A: TABLE OF PARAMETERS

Values of the 40-parameter surface [see Eq. (16) for the definition of the surface and use of the parameters] are shown in Table I.

APPENDIX B: PHASE AVERAGING

In the calculation of the surface generated from the mean of the parameters, the average cannot be taken directly due to wrapping of the phase parameters in the trace. The angular mean is used for the surface phase parameters, and is calculated by

$$\bar{\theta} = \tan^{-1}\left(\frac{\sum_i \sin(\theta_i)}{\sum_i \cos(\theta_i)}\right). \tag{B1}$$

This calculation takes into account wrapping of the phase in $(0, 2\pi)$ and should yield an expected average value.

[1]G. Dolcetti, A. Krynkin, K. V. Horoshenkov, and S. J. Tait, "An acoustic technique to measure the velocity of shallow turbulent flows remotely," in *Free Surface Flows and Transport Processes, 36th International School of Hydraulics* (Springer, Berlin, 2018), pp. 181–194.

[2]A. Nichols, S. Tait, K. Horoshenkov, and S. Shepherd, "A non-invasive airborne wave monitor," Flow Meas. Instrum. **34**, 118–126 (2013).

[3]S. P. Walstead and G. B. Deane, "Reconstructing surface wave profiles from reflected acoustic pulses using multiple receivers," J. Acoust. Soc. Am. **136**(2), 604–613 (2014).

[4]L. Hellequin, J.-M. Boucher, and X. Lurton, "Processing of high-frequency multibeam echo sounder data for seafloor characterization," IEEE J. Ocean. Eng. **28**(1), 78–89 (2003).

[5]A. Krynkin, K. V. Horoshenkov, and T. Van Renterghem, "An airborne acoustic method to reconstruct a dynamically rough flow surface," J. Acoust. Soc. Am. **140**(3), 2064–2073 (2016).

[6]A. Krynkin, G. Dolcetti, and S. Hunting, "Acoustic imaging in application to reconstruction of rough rigid surface with airborne ultrasound waves," Rev. Sci. Instrum. **88**(2), 024901 (2017).

[7]N. J. Joslyn and D. R. Dowling, "Recovery of coherent reflection from rough-surface scattered acoustic fields via the frequency-difference autoproduct," J. Acoust. Soc. Am. **151**(1), 620–633 (2022).

[8]M. Kleiner, H. Gustafsson, and J. Backman, "Measurement of directional scattering coefficients using near-field acoustic holography and spatial transformation of sound fields (P)," J. Audio Eng. Soc. **45**(5), 331–346 (1997), available at https://aes2.org/publications/elibrary-page/?id=7648.

[9]A. Richard, D. Fernández Comesaña, J. Brunskog, C.-H. Jeong, and E. Fernandez-Grande, "Characterization of sound scattering using near-field pressure and particle velocity measurements," J. Acoust. Soc. Am. **146**(4), 2404–2414 (2019).

[10]G. Dolcetti, M. Alkmim, J. Cuenca, L. De Ryck, and A. Krynkin, "Robust reconstruction of scattering surfaces using a linear microphone array," J. Sound Vib. **494**, 115902 (2021).

[11]J. Ogilvy, "Wave scattering from rough surfaces," Rep. Prog. Phys. **50**(12), 1553 (1987).

[12]M.-D. Johnson, A. Krynkin, G. Dolcetti, M. Alkmim, J. Cuenca, and L. De Ryck, "Surface shape reconstruction from phaseless scattered acoustic data using a random forest algorithm," J. Acoust. Soc. Am. **152**(2), 1045–1057 (2022).

[13]M. J. Bianco, P. Gerstoft, J. Traer, E. Ozanich, M. A. Roch, S. Gannot, and C.-A. Deledalle, "Machine learning in acoustics: Theory and applications," J. Acoust. Soc. Am. **146**(5), 3590–3628 (2019).

[14]C. Andrieu, N. De Freitas, A. Doucet, and M. I. Jordan, "An introduction to MCMC for machine learning," Mach. Learn. **50**(1), 5–43 (2003).

[15]S. Yu, B. Liu, K. Yu, Z. Yang, G. Kan, and L. Zong, "Inversion of bottom parameters using a backscattering model based on the effective density fluid approximation," Appl. Acoust. **182**, 108187 (2021).

[16]A. E. Fouda and F. L. Teixeira, "Bayesian compressive sensing for rough surface reconstruction," in *2021 IEEE 19th International Symposium on Antenna Technology and Applied Electromagnetics (ANTEM)* (IEEE, New York, 2021), pp. 1–2.

[17]J. Antoni, Q. Leclere, and T. Lemagueresse, "Sparse holography from iterated Bayesian focusing," in *INTER-NOISE and NOISE-CON Congress and Conference Proceedings* (Institute of Noise Control Engineering, Wakefield, MA, 2018), Vol. 257, pp. 648–659.

[18]T. Le Magueresse, J.-H. Thomas, J. Antoni, and S. Paillasseur, "Instantaneous bayesian regularization applied to real-time near-field acoustic holography," J. Acoust. Soc. Am. **142**(2), 924–934 (2017).

[19]Z. Li, Y. Liu, J. Sun, and L. Xu, "Quality-bayesian approach to inverse acoustic source problems with partial data," SIAM J. Sci. Comput. **43**(2), A1062–A1080 (2021).

[20]Z. Yang, X. Gui, J. Ming, and G. Hu, "Bayesian approach to inverse time-harmonic acoustic scattering with phaseless far-field data," Inverse Prob. **36**(6), 065012 (2020).

[21]Z. Yang, X. Gui, J. Ming, and G. Hu, "Bayesian approach to inverse time-harmonic acoustic obstacle scattering with phaseless data generated by point source waves," Comput. Methods Appl. Mech. Eng. **386**, 114073 (2021).

[22]A. Palafox, M. A. Capistrán, and J. A. Christen, "Effective parameter dimension via Bayesian model selection in the inverse acoustic scattering problem," Math. Probl. Eng. **2014**, 427203.

[23]M.-H. Chen, Q.-M. Shao, and J. G. Ibrahim, *Monte Carlo Methods in Bayesian Computation* (Springer Science & Business Media, Berlin, 2012).

[24]T. Hong and M. K. Sen, "A new MCMC algorithm for seismic waveform inversion and corresponding uncertainty analysis," Geophys. J. Int. **177**(1), 14–32 (2009).

[25]I. Smal, N. Carranza-Herrezuelo, S. Klein, W. Niessen, and E. Meijering, "Trans-dimensional MCMC methods for fully automatic motion analysis in tagged MRI," in *Medical Image Computing and Computer-Assisted Intervention 2011* (Springer, Berlin, Heidelberg, 2011), Vol. 6891, pp. 573–580, available at https://scholar.google.com/scholar?hl=en&as_sdt=0%2C5&q=Trans-dimensional+MCMC+methods+for+fully+automatic+motion+analysis+715+in+tagged+MRI&btnG=#d=gs_cit&t=1733512558697&u=%2Fscholar%3Fq%3Dinfo%3AKV8IKLWnYCgJ%3Ascholar.google.com%2F%26output%3Dcite%26scirp%3D0%26hl%3Den.

[26]I. Smal, N. Carranza-Herrezuelo, S. Klein, P. Wielopolski, A. Moelker, T. Springeling, M. Bernsen, W. Niessen, and E. Meijering, "Reversible jump MCMC methods for fully automatic motion analysis in tagged MRI," Med. Image Anal. **16**(1), 301–324 (2012).
[27]M. Niskanen, J.-P. Groby, A. Duclos, O. Dazel, J. Le Roux, N. Poulain, T. Huttunen, and T. Lähivaara, "Deterministic and statistical characterization of rigid frame porous materials from impedance tube measurements," J. Acoust. Soc. Am. **142**(4), 2407–2418 (2017).
[28]S. G. Konarski, C. A. Rohde, R. Gotoh, S. N. Roberts, and C. J. Naify, "Acoustic measurement and statistical characterization of direct-printed, variable-porosity aluminum foams," J. Acoust. Soc. Am. **149**(6), 4327–4336 (2021).
[29]H. Haario, E. Saksman, and J. Tamminen, "An adaptive Metropolis algorithm," Bernoulli **7**, 223–242 (2001).
[30]E. I. Thorsos, "The validity of the Kirchhoff approximation for rough surface scattering using a Gaussian roughness spectrum," J. Acoust. Soc. Am. **83**(1), 78–92 (1988).
[31]P. M. Morse and K. U. Ingard, *Theoretical Acoustics* (Princeton University Press, Princeton, NJ, 1986).
[32]J. Joyce, "Bayes' theorem" (2003).
[33]H. Haario, E. Saksman, and J. Tamminen, "Adaptive proposal distribution for random walk Metropolis algorithm," Comput. Stat. **14**, 375–396 (1999).
[34]C. Andrieu and J. Thoms, "A tutorial on adaptive MCMC," Stat. Comput. **18**(4), 343–373 (2008).
[35]J. Kaipio and E. Somersalo, *Statistical and Computational Inverse Problems* (Springer-Verlag, Berlin, 2005).
[36]G. Dolcetti and A. Krynkin, "Doppler spectra of airborne ultrasound forward scattered by the rough surface of open channel turbulent water flows," J. Acoust. Soc. Am. **142**(5), 3122–3134 (2017).
[37]O. M. Phillips, "The equilibrium range in the spectrum of wind-generated waves," J. Fluid Mech. **4**(4), 426–434 (1958).
[38]D. R. Jackson, D. P. Winebrenner, and A. Ishimaru, "Application of the composite roughness model to high-frequency bottom backscattering," J. Acoust. Soc. Am. **79**(5), 1410–1422 (1986).
[39]M. T. Stewart, S. M. Cameron, V. I. Nikora, A. Zampiron, and I. Marusic, "Hydraulic resistance in open-channel flows over self-affine rough beds," J. Hydraulic Res. **57**(2), 183–196 (2019).
[40]G. Dolcetti, K. Horoshenkov, A. Krynkin, and S. Tait, "Frequency-wavenumber spectrum of the free surface of shallow turbulent flows over a rough boundary," Phys. Fluids **28**(10), 105105 (2016).
[41]D. Foreman-Mackey, "corner. py: Scatterplot matrices in python," J. Open Source Software **1**(2), 24 (2016).
[42]J. Cuenca, T. Lähivaara, M.-D. Johnson, G. Dolcetti, M. Alkmim, "L. De Ryck, and A. Krynkin, A statistical inverse method for the reconstruction of rough surfaces from acoustic scattering" (2023).
[43]M. Betancourt, "A conceptual introduction to Hamiltonian Monte Carlo," arXiv:1701.02434 (2017).